Supplementary Information (SI) for Journal of Materials Chemistry C.

SUPPLEMENTARY INFORMATION

Mechanistic Insight into the Nitrogen Photofixation Reaction by BiOBr-based Heterojunctions

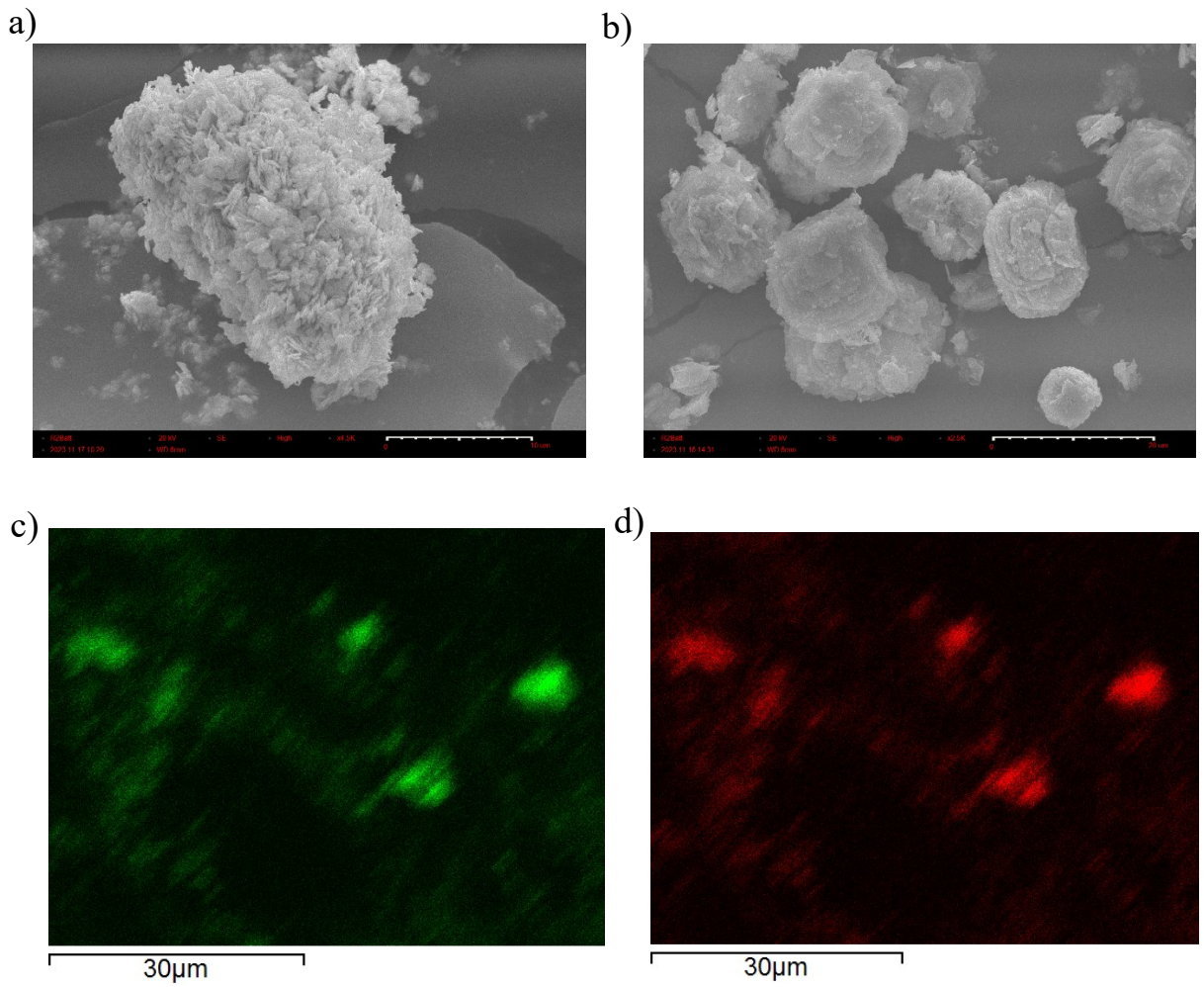

Figure S1. Representative SEM images of a) BiOBr; b) BiOBr10%/g-CN 90% (best performing composite for ammonia photogeneration; c) Bi and d) Br elemental maps of BiOBr10%/g-CN 90% .

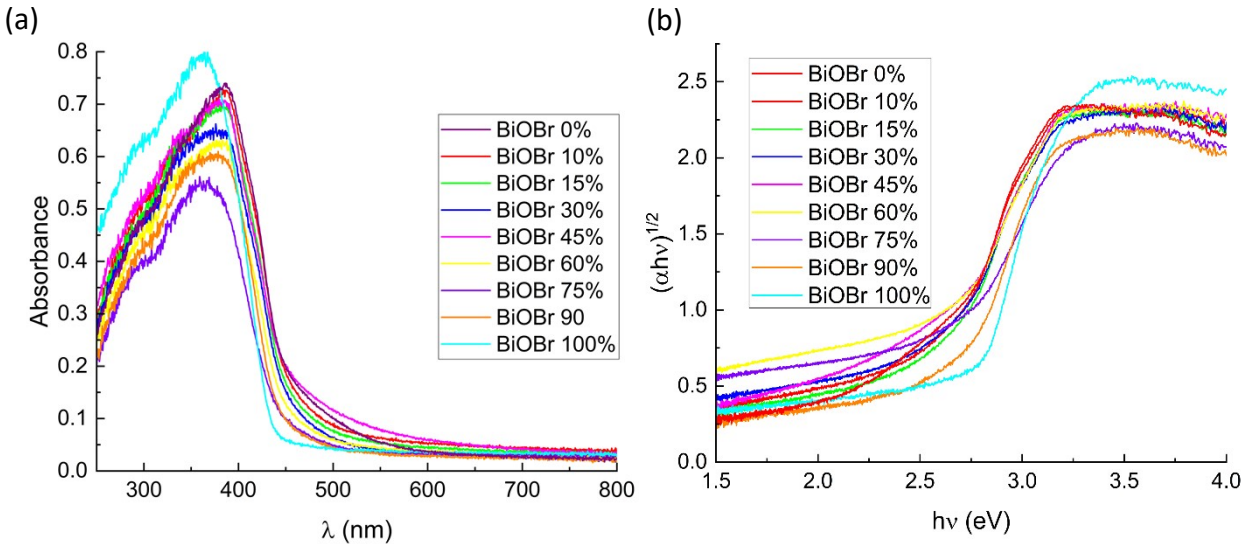

Figure S2. a) Absorption spectra and b) Tauc plots for samples of the BiOBr/g-CN system.

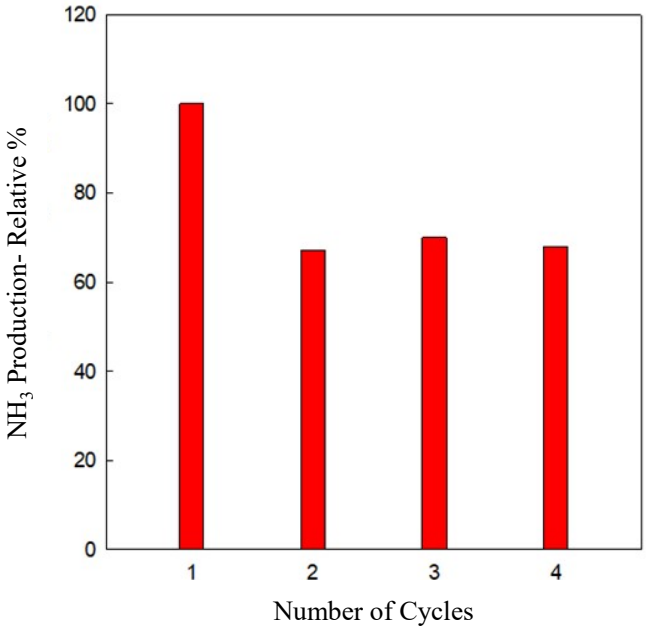

Figure S3. Trend over four cycles for the best performing composite, namely BiOBr 10 wt%/g-CN 90 wt%.

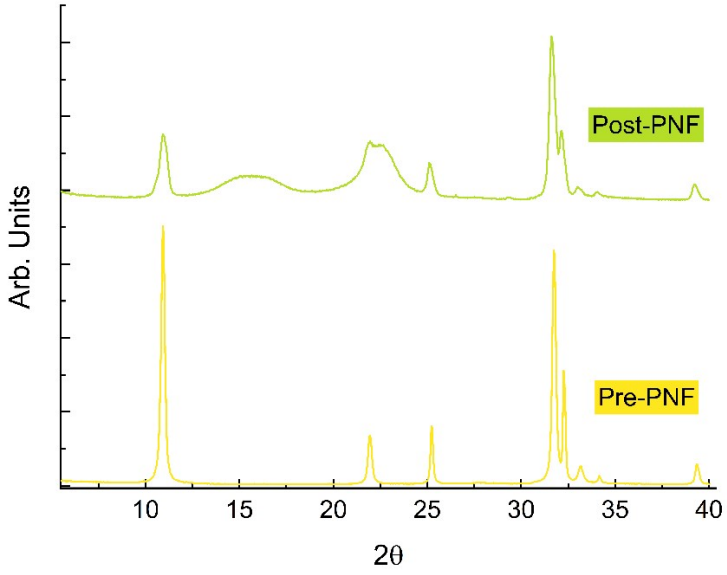

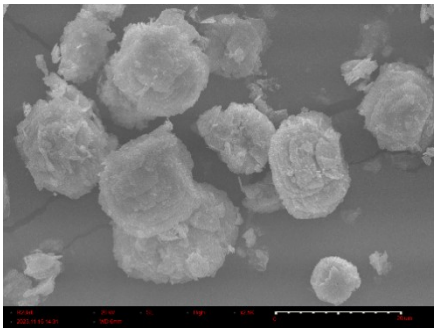

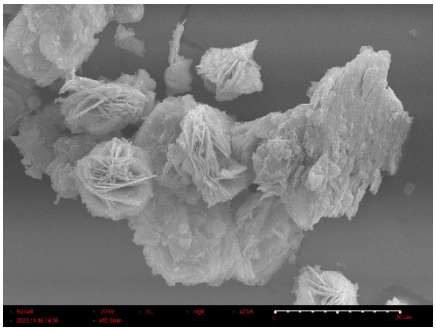

Figure S4. a) XRD of the BiOBr 10 wt%/g-CN 90 wt% before and after the photocatalysis; b) and c) are illustrative images of BiOBr 10 wt%/g-CN 90 wt% bedore and after the photocatalytic test.

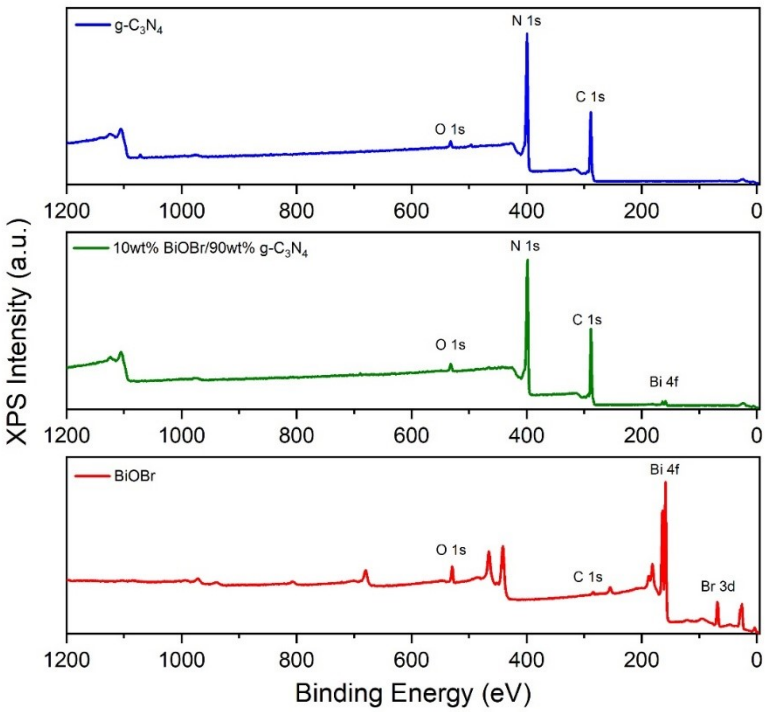

Figure S5: Comparison of the wide scans collected on the three analysed samples – from top to bottom: *g*-C_3N_4, BiOBr 10 wt%/g-CN 90 wt%, and BiOBr.

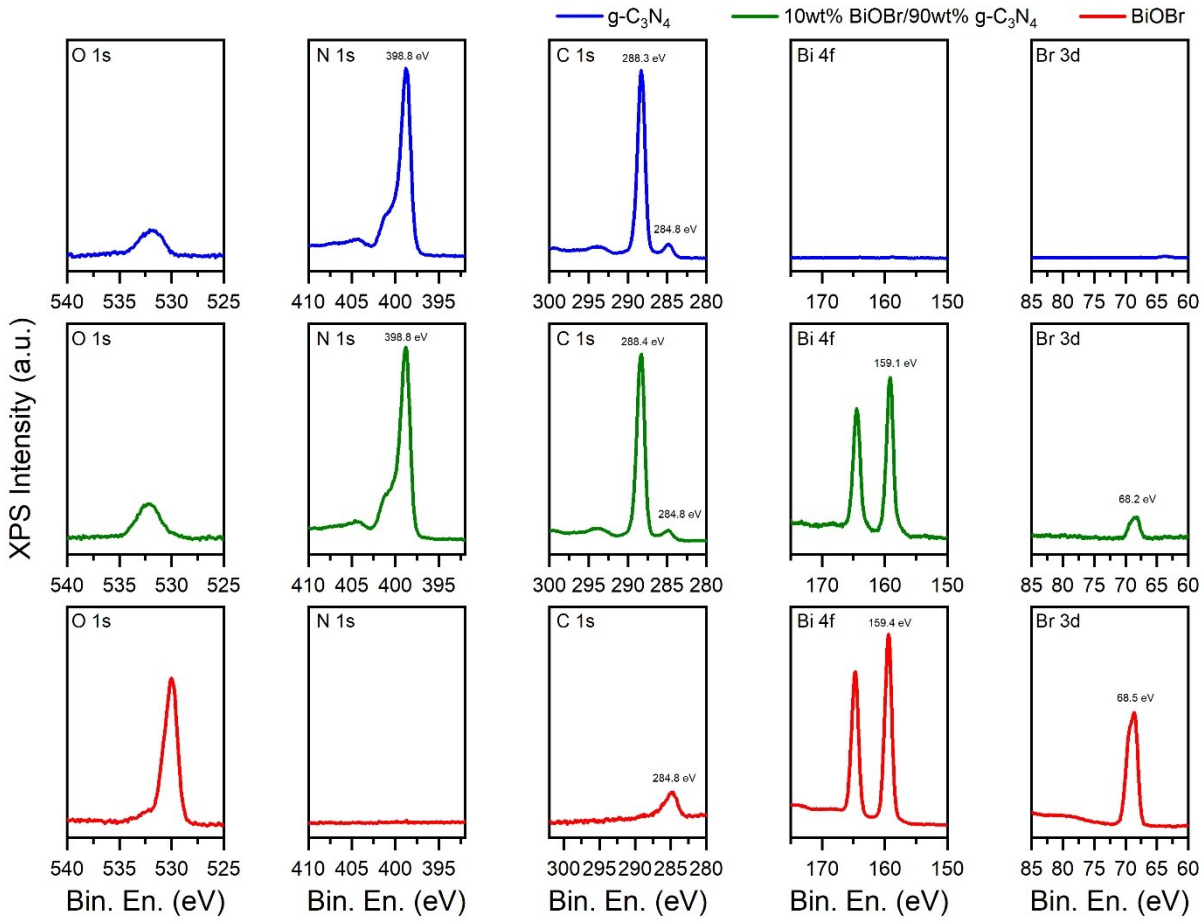

Figure S6: Comparison of the high-resolution spectra collected on the three analysed samples – from top to bottom: *g*-CN, BiOBr 10 wt%/g-CN 90 wt%, and BiOBr.

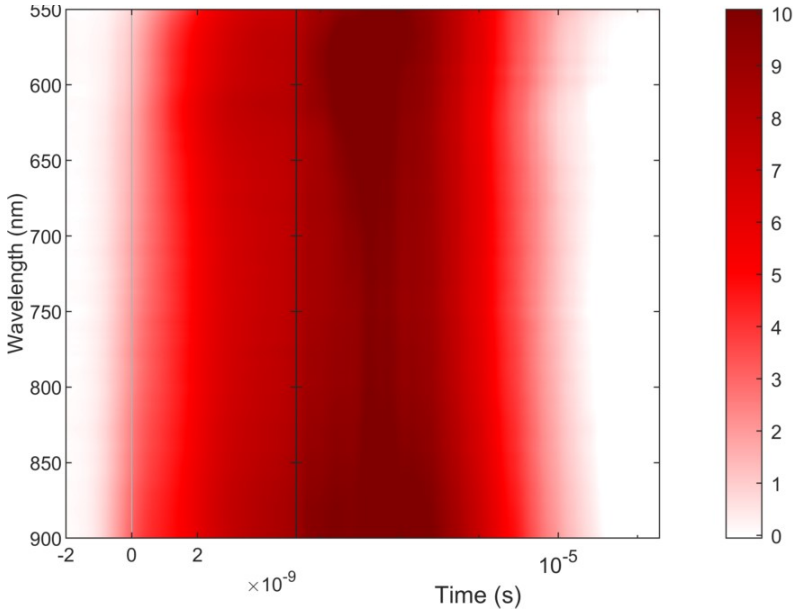

Figure S7 2D map representing the transient absorption measurements taken on BiOBr sample, in a wavelength range between 550 and 900 nm and in a time range up to 25 μs.

Table S1 Indirect band-gap values for the BiOBr/g-CN composites extracted from the Tauc plots.

BiOBr %	Indirect E_g (eV)
0	2.49
10	2.50
15	2.49
30	2.45
45	2.36
60	2.36
75	2.42
90	2.46
100	2.68

Experimental Section

Sample synthesis and characterization

Nanosheets g-C_3N_4 has been synthesized from the bulk form (bulk g-C_3N_4) with a polymerization of Dicyandiamine DCD ($NH_2C(=NH)NHCN$, Aldrich, 99%) by the following thermal treatment under N_2 flux: heating (1 °C min^{-1}) to a selected temperature of 550 °C, the isothermal step for 4 hours followed by cooling to room temperature (10 °C min^{-1}). The synthesis was carried out in a partially closed alumina crucible. The thermal exfoliated catalyst (nanosheets) was prepared by heating to a selected temperature of 500 °C with an isothermal step for 2h the bulk g-C_3N_4 in air. The BiOBr/nanosheets g-C_3N_4 composite has been synthesized dissolving a stoichiometric ratio of the precursors salt. The composites series have been realized changing the percentage of the BiOBr and the nanosheets g-C_3N_4 (g-C_3N_4) in the composites: 100, 90, 75, 60, 45, 30, 15, 10. For each composition, three independent syntheses made in different days has been collected in a single batch.

The crystal structure of the samples has been characterized by room temperature Cu-radiation XRD acquired with Bruker D2 diffractometer. DRS spectra were acquired in the wavelength range 300-800 nm directly on the powders by using a Jasco V-750 spectrophotometer, equipped with an integrating sphere (Jasco ISV-922). Microstructural characterization of the samples was made using a high-resolution scanning electron microscope (SEM, TESCAN Mira 3) operated at 25 kV.

Nitrogen Photofixation Experiments and Ammonia Determination

N_2 photofixation experiments were conducted in tridistilled water containing 10% (v/v) methanol (Aldrich, ≥99.9%) irradiated in Pyrex glass container (250 mL capacity, 100 mL

sample). The methanol plays the role of sacrificial agent. The electrons produced in the photocatalyst migrate from the bulk to the surface of the material to reduce H_2O to H_2, to minimize the recombination of electrons-holes a sacrificial agent is employed to be oxidated faster that water to avoid the rapid recombination electron-hole and to maximize the electron extraction. After addition of the catalyst (0.5 g L^{-1}), the sample suspension was deoxygenated by N_2 bubbling (45 min) to obtain a saturated solution and then irradiated under magnetic stirring for 3 hours maintaining the temperature at 15°C. For each BiOBr/g-CN composite, the experiments (n =3) have been performed on a single batch obtained from three independent syntheses made in different days. The quantification was performed with ammonia ion selective electrode (ISE), which guarantees accurate detection over colorimetric methods (e.g. Nessler method) as previously assessed.[1,2] The pH of all standards and samples was adjusted above 11 with a strong base (10 N NaOH, ion strength < 1M), so that dissolved ammonia (NH_3(aq) and NH_4^+) is converted to NH_3(aq). A calibration curve was daily constructed (0.1- 25 mg L^{-1} NH_3) plotting the mV value recorded after 2 min equilibration time against the Log Concentration, to verify the slope (varying in the range - 54 ÷ -60 mV). Figure S8 reports an example of mean calibration curve (0.1 mg L^{-1} ÷ 25 mg L^{-1} as NH_3). The ammonia concentration in the sample was further confirmed by two standard additions on the sample.

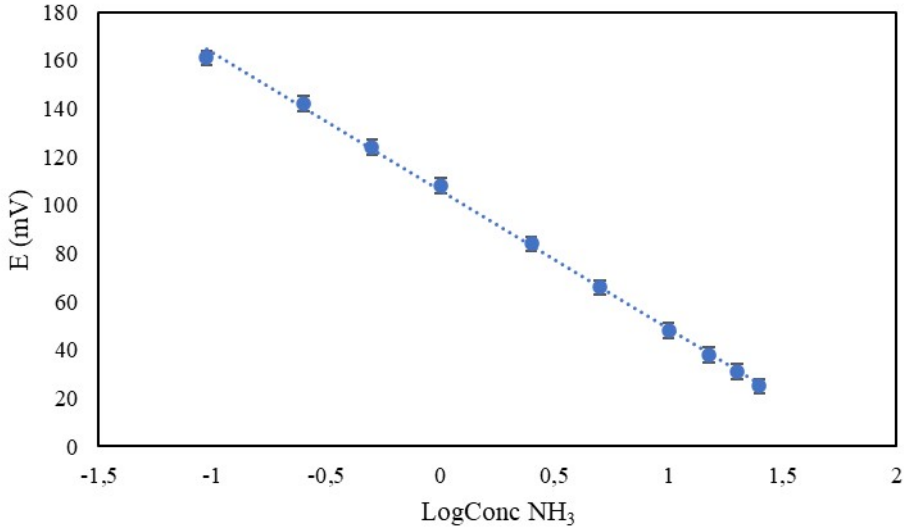

Figure S8. Mean calibration curve (n=7) for ammonia quantification (0.1 mg L^{-1} ÷ 25 mg L^{-1} as NH_3).

Optical Spectroscopic characterization

Transient absorption spectroscopy (TAS) measurements were performed in transmission mode on powder samples dispersed in DMF with a concentration of 5 mg/ml. A femtosecond laser (Light Conversion Pharos) generates pulses of 280 fs centered at 1030 nm. Focusing a part of this fundamental beam on a sapphire plate a broadband white light was generated, spanning from 520 to 900 nm, which was used as probe beam. At short delays (<3 ns), the pump beam was generated from the third harmonic of the fundamental providing a wavelength of 343nm. At long delays (>3 ns), we used a Q-switched Nd YVO4 laser (Innolas Picolo) to generate a 355nm pump beam electronically triggered to control the delay between pump and probe. Photoluminescence (PL) measurements were conducted by using the same pump used for fs-TAS measurements (343nm), the emission is then collected by a Maya 2000 pro spectrometer from Ocean Optics.

XPS Analysis

X-ray Photoelectron Spectroscopy (XPS) was used to study the surface chemistry of the BiOBr 10 wt%/g-CN 90 wt% optimized system in comparison to that of the composing materials, namely *g*-C_3N_4 and BiOBr. XPS specimens were prepared by pressing a few mg of the powder samples onto high-purity indium pellets (99.99% purity). XPS data were acquired using a Kratos Axis Ultra^{DLD} spectrometer, equipped with a monochromatic Al Kα source operated at 20 mA and 15 kV. Wide scan were acquired at a pass energy of 160 eV, energy step of 1 eV, over an analysis area of 300 x 700 μm^2. High-resolution spectra were then acquired at a pass energy of 20 eV, energy step of 0.1 eV, over the same analysis area, with a specific focus on the main signals from the elements composing the materials, namely O 1s, C 1s, N 1s, Bi 4f, and Br 3d. The Kratos charge neutralizer system was used on all specimens; spectra have been charge corrected by setting the lowest binding-energy component of the carbon 1s spectrum to 284.8 eV. The collected data were then analysed with CasaXPS software (version 2.3.24).[3]

Computational Modelling

We here aim at aligning the electronic energy levels of g-C_3N_4 and BiOBr with respect to the relevant reduction potentials at the semiconductor-water interface. For the former material, we employ the results of the alignment detailed in Ref 1.[4] The latter is calculated in this work, as follows.

First, we recall that the fundamental band gap of a semiconductor at a temperature T, as calculated from first principles, $E_g^{theory}(T)$, can be defined as:

$$E_g^{theory}(T) = E_g^{theory}(0) + \Delta E_g(T),$$

where $E_g^{theory}(0)$ is calculated band gap at 0 K, usually estimated employing an electronic-structure calculation on the perfectly ordered crystalline system.[5] For materials including heavy atoms, such as Bi and I, this calculation needs to include the effect of spin-orbit coupling (SOC), which are known to produce a sizable renormalization of the band gap in Bi-based materials, e.g. Ref. 2, $\Delta E_g(SOC)$, as a consequence of the shifts in the position of the valence band maximum (VBM) and conduction band minumum (CBM), $\Delta E_{VBM}(SOC)$ and $\Delta E_{CBM}(SOC)$, respectively. $\Delta E_g(T)$ is the thermal band gap

renormalization ensuing form atomic vibrations at finite temperatures, which has beend found to be particularly significant for a plethora of systems, including fully inorganic perovskites, Bi-based semiconductors, and organic materials.[5–7] The individual contribution to the total band gap renormalization deriving from the valence band maximum (VBM) and conduction band minimum (CBM) are similarly defined:

$$E_{VBM}^{theory}(T) = E_{VBM}^{theory}(0) + \Delta E_{VBM}(T)$$
$$E_{CBM}^{theory}(T) = E_{CBM}^{theory}(0) + \Delta E_{CBM}(T)$$

In the following, we describe the computational protocol employed to calculate band gap at room temperature from electronic-structure calculations and how to align the calculated energy levels with respect to a physical reference.

We model BiOBr and, for comparison, the oxyiodide with analogous structure, BiOI, employing a supercell approach. In particular, we consider $5 \times 5 \times 3$ tetragonal supercells with $a = b = 19.60$ Å, $c = 24.33$ Å for BiOBr and $a = b = 20.05$ Å, $c = 27.42$ Å for BiOI, see Figure S8, corresponding to the experimental density. Most of the calculations based on density functional theory (DFT) are carried out with the freely available CP2K/QUICKSTEP suite of programs.[8] In this code, atomic basis sets are combined with an auxiliary plane-wave basis set to re-expand the electron density. In particular, we use the MOLOPT double-zeta polarized basis set and a cutoff of 800 Ry for the plane waves.[9] Core electrons are treated with the analytical Goedecker-Teter-Hutter pseudopotentials.[10] The Brillouin zone is sampled at the sole Γ point. To properly calculate the band gap and the band edges of the materials under study, we employ a piece-wise linear hybrid functional belonging to the PBE0 family, PBE(α_K), developed in Ref. 10, where fractions α_K of Fock exchange equal to 23% and 24% have been found to satisfy the generalized Koopmans' condition for BiOBr and BiOI, respectively.[11–14] We employ the auxiliary density matrix method to speed up the calculation of exact exchange in hybrid functional calculations, as implemented in CP2K, with the cFIT auxiliary basis set. Furthermore, we include non-local electron correlation via the self-consistent rVV10 scheme, to accurately describe the energetics of layered materials.[15–17]

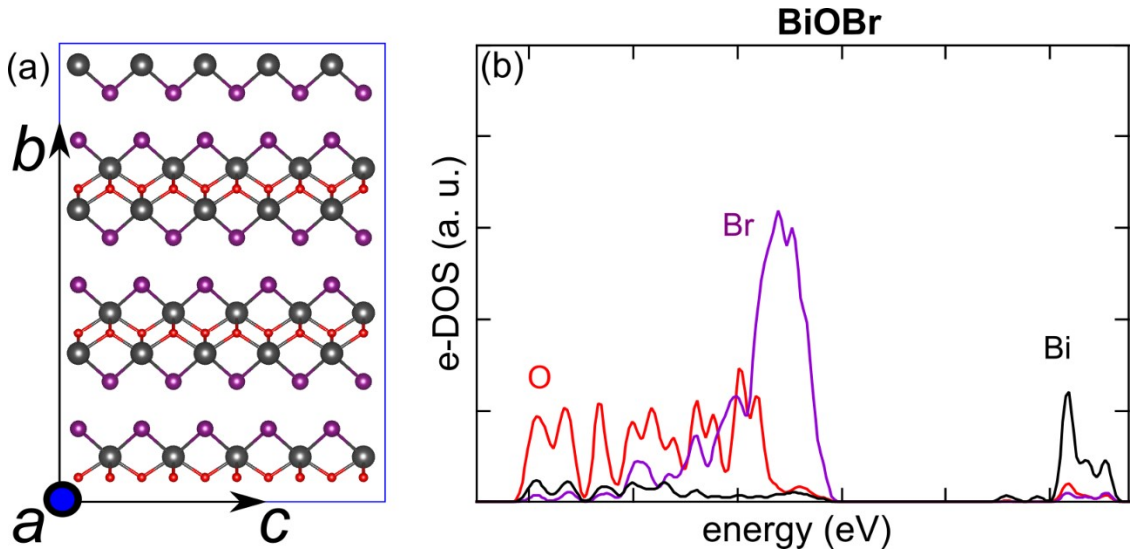

Figure S9. (a) Stick&Ball representation of the $5 \times 5 \times 3$ tetragonal supercell employed to model BiOX materials. O is in red, X = Br, I in purple, and Bi in grey. (b) Electronic density of states (e-DOS) calculated for bulk BiOBr.

Since the band edges of BiOX are dominated by the 2p states of the halogen and Bi 6s states (valence band) and Bi 6p states (conduction band), see Figure S9 (b) for BiOBr, we need to evaluate the shift of the band edges and the subsequent renormalization of the band gap induced by spin-orbit coupling.[18] For this reason, we carry out hybrid density functional theory calculations with and without the effect within the VASP code.[12,13,14] The calculations are performed on a 6-atom unit cell using a Γ-centered 4×4×4 Monkhorst–Pack k-point mesh. The plane-wave cutoff energy is 520 eV. SOC-induced band edge shifts is computed as the difference between calculations with and without SOC. All calculations are performed at fixed experimental lattice parameters, without structural optimization. From the difference in the absolute position of the band edges calculated with and without SOC, we infer the values of $\Delta E_g(SOC)$, $\Delta E_{VBM}(SOC)$, and $\Delta E_{CBM}(SOC)$ for both materials, as collected in Table S1.

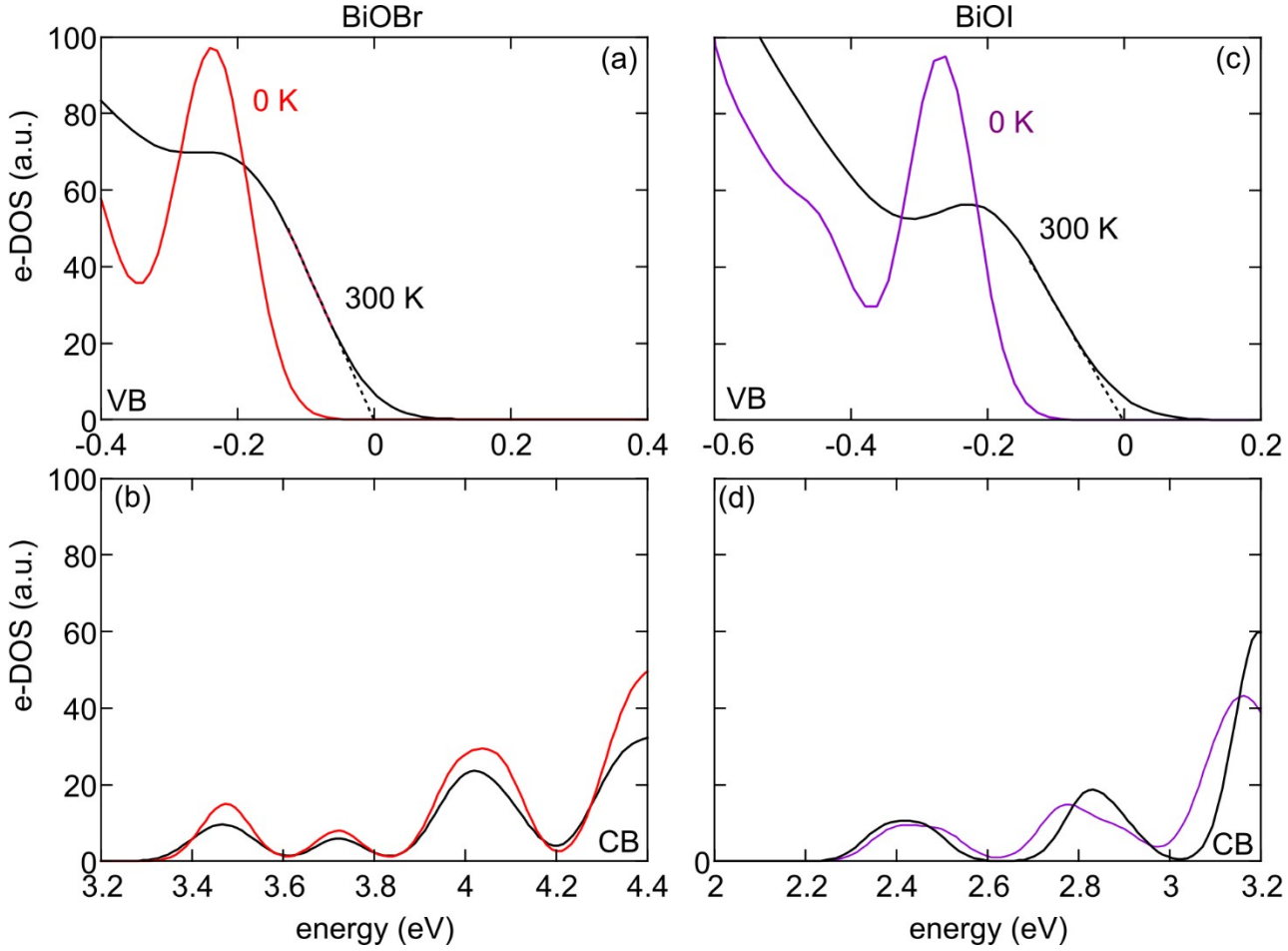

Figure S10. Electronic density of states (e-DOS) near the band edges for BiOBr (a, b) and BiOI (b. c). Black solid lines for DOS achieved from MD at 300 K. Red (purple) lines for DOS calculated from the optimized structures at 0 K of BiOBr (BiOI). For each material, energy levels are referred to the room-temperature valence band maximum, as estimated from linear extrapolation of the wing of the e-DOS.

Finally, the renormalization due to thermal motions is known to substantially impact the room-temperature band gap of a variety of semiconductors, including organic materials, halide perovskites, and Bi-based semiconductors.[5–7] For this reason, we perform molecular dynamics (MD) simulations with CP2K/QUICKSTEP using the same computational set-up described above. MD runs in the canonical NVT ensemble, ensured by the use of the thermostat developed by Nosé and Hoover, are carried out for 10 picoseconds, with a time-step of 1 fs.[22,23] We then employ a linear extrapolation of the wings of the electronic density of states (DOS) near the band edges. The difference in the band edges calculated at 0 K and those achieved from the MD simulation at 300 K provides us with the estimated values of $\Delta E_g(T)$, $\Delta E_{VBM}(T)$, $\Delta E_{CBM}(T)$ cf. Figure S10 and Table S2. The slightly larger value observed for BiOI can be ascribed to the wider thermal fluctuactions of the Bi-I bonds, as evidenced by the calculated radial distribution functions in Figure S11.

Table S2. Calculated values of the SOC and thermal corrections to the band edges and to the fundamental band gap of the considered BiOX semiconductors. All values are given in eV.

Correction	BiOBr	BiOI
$\Delta E_{VBM}(SOC)$	+ 0.02	+ 0.12
$\Delta E_{CBM}(SOC)$	− 0.21	− 0.20
$\Delta E_{g}(SOC)$	− 0.23	− 0.32
$\Delta E_{VBM}(T)$	+ 0.12	+ 0.14
$\Delta E_{CBM}(T)$	− 0.05	− 0.12
$\Delta E_{g}(T)$	− 0.17	− 0.26

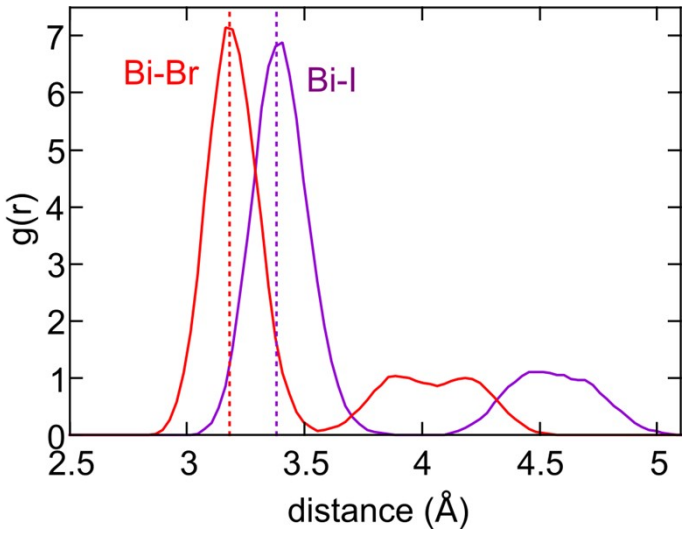

Figure S11. Bi-X radial distribution functions (X=I, Br) as calculated from MD simulations of BiOX materials. Bi-Br in violet, Bi-I in red. Vertical dashed line represent the lengths of Bi-X bonds for the respective optimized 0 K atomistic models.

To align the calculated band edges with respect to a physical reference, we model BiOX-vacuum interfaces. In particular, we construct atomistic slabs of BiOBr and BiOI, considering two different stoichiometric symmetric systems: the (001) and the (010) surfaces. The bulk-like (001) surface is cut in parallel with respect to the BiOX layered planes and it is BiX-terminated with no undercoordinated atoms, as illustrated in Figure 6. The slab has $a = b = 15.68$ Å, $c = 70.00$ Å for BiOBr and $a = b = 16.04$ Å, $c = 70.00$ Å for BiOI (including, for both BiOBr and BiOI, ~30 Å of vacuum) and consists of 5 BiOX layers. We note that for the (001) surface, we also tested O-

terminated surfaces, which, however, resulted in unstable systems, with disruption of the terminal unsaturated layers. The same occurred when considering O-H covered, i.e. hydroxylated, slabs.

At variance with this, the stoichiometric (010) slab displays a BiOX-terminated surface perpendicular to the direction of the layered planes and features undercoordinated atoms, cf. Figure 5. The dimensions of the periodic slabs are $a = 16.22$ Å, $b = 15.68$ Å, $c = 75.00$ Å for BiOBr and $a = 18.22$, $b = 16.04$ Å, $c = 75.00$ Å for BiOI, again with a vacuum layer of ~30 Å, separating the periodic replicas along the z direction. For each slab, we carry out a full geometry relaxation at the PBE(α_K)+rVV10 level of theory.

The surface energies of the slabs are calculated according to the following expression:

$$\gamma = \frac{(E_{slab} - N \times E_{bulk})}{2A},$$

where E_{slab} is the total energy of the slab, E_{bulk} the total energy *per atom* of the bulk, and A is the surface area of the slab model. As reported in Table S3, surface energies are found to amount to 0.011 and 0.048 eV/Å^2 for the (001) and the (010) surface models of BiOBr, respectively. Similar values of 0.011 and 0.028 eV/Å^2 are estimated for BiOI surfaces, which, however, shows a reduced difference between the two surface terminations.

Table S3. Calculated values of the surface energy γ from atomistic modelling of the (001) and the (010) surfaces for the BiOX semiconductors under consideration. Values are given in eV/Å^2.

	BiOBr	BiOI
γ_{001}	0.011	0.011
γ_{010}	0.048	0.028

For each slab, we determine the plane-averaged electrostatic-potential along the z direction, to refer the calculated band edges with respect to the vacuum level. No residual electrical field is observed in the studied slabs, as evidenced by the flat potential across the vacuum region shown in Figure S12. Finally, we align the calculated energy levels also with respect to the standard hydrogen electrode (SHE), since redox potentials are usually reported on this energy scale. In particular, for internal consistence, we employ a computational SHE detailed in Refs. 24 and 25, which is found 4.56 eV below the vacuum level, in excellent accord with the experimental estimate proposed by Trasatti (4.44 eV).[24–26] The alignment scheme presented in Fig. 6 of the main text is completed including the experimental reference values for N_2/NH_3 and O_2/H_2O redox levels.

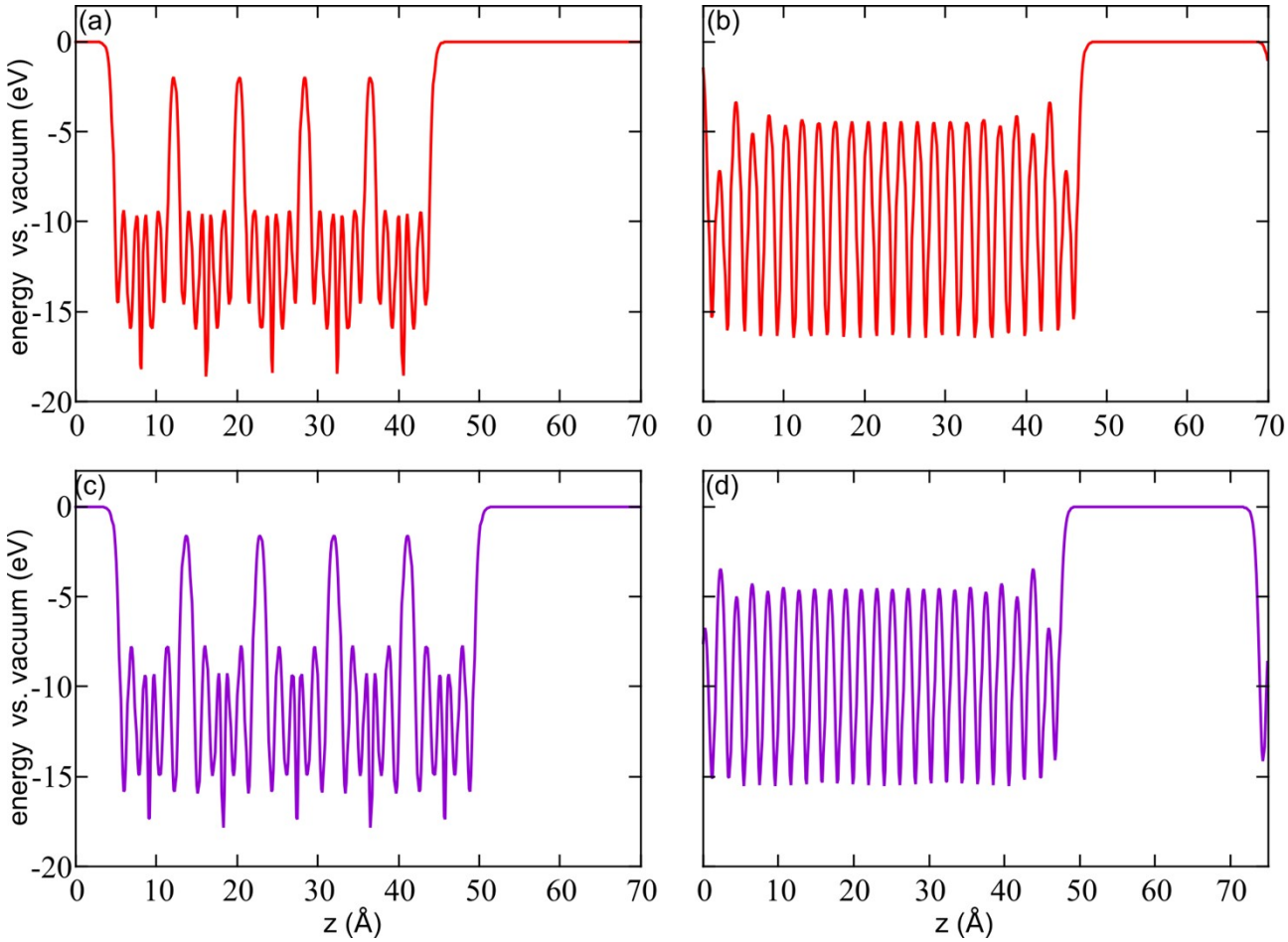

Figure S12. Average electrostatic potential referred to the vacuum level across the semiconductor-vacuum interface for BiOBr and BiOI (red and purple lines respectively). Panels (a) and (c) for models of (001) surface while panels (b) and (d) illustrate the potential profile for (010) slabs.

In the main text, we also report the energy level associated with surface polarons on the (010) surface. The binding energy of the electron polaron is defined as:

$$E_b^-(pol) = E_{slab}^-(pristine) - E_{slab}^-(pol)$$

where $E_{slab}^-(pol)$ is the total energy of the charged slab with the polaronic distortion, while $E_{slab}^-(pristine)$ the total energy of the charged pristine slab. A positive value of the quantity corresponds to favorable polaronic localization. The redox level $(0/-1)$ associated with the polaron, $\mu(0/-1)$, is placed at an energy $E_b^-(pol)$ below the position of the conduction band maximum, ϵ_{CBM}, of the material, i.e.:

$$\mu(0/-1) = \epsilon_{CBM} - E_b^-(pol)$$

References

1 C. Tedesco, L. Gregori, A. Simbula, F. Pitzalis, A. Speltini, F. Merlo, S. Colella, A. Listorti, E. Mosconi, A. A. Alothman, W. Kaiser, M. Saba, A. Profumo, F. De Angelis and L. Malavasi, *Adv Energy and Sustain Res*, 2024, 2400040.
2 C. Tedesco, A. Simbula, R. Pau, F. Merlo, A. Speltini, V. Armenise, A. Listorti, L. Gregori, A. A. Alothman, E. Mosconi, M. Saba, A. Profumo and L. Malavasi, *Solar RRL*, 2025, **9**, 2400778.
3 N. Fairley, V. Fernandez, M. Richard-Plouet, C. Guillot-Deudon, J. Walton, E. Smith, D. Flahaut, M. Greiner, M. Biesinger, S. Tougaard, D. Morgan and J. Baltrusaitis, *Applied Surface Science Advances*, 2021, **5**, 100112.
4 L. Romani, A. Speltini, F. Ambrosio, E. Mosconi, A. Profumo, M. Marelli, S. Margadonna, A. Milella, F. Fracassi, A. Listorti, F. De Angelis and L. Malavasi, *Angewandte Chemie International Edition*, 2021, **60**, 3611–3618.
5 J. Wiktor, I. Reshetnyak, F. Ambrosio and A. Pasquarello, *Phys. Rev. Materials*, 2017, **1**, 022401.
6 J. Wiktor, U. Rothlisberger and A. Pasquarello, *J. Phys. Chem. Lett.*, 2017, **8**, 5507–5512.
7 F. Ambrosio, J. Wiktor, A. Landi and A. Peluso, *J. Phys. Chem. Lett.*, 2023, **14**, 3343–3351.
8 J. VandeVondele, M. Krack, F. Mohamed, M. Parrinello, T. Chassaing and J. Hutter, *Computer Physics Communications*, 2005, **167**, 103–128.
9 J. VandeVondele and J. Hutter, *The Journal of Chemical Physics*, 2007, **127**, 114105.
10 S. Goedecker, M. Teter and J. Hutter, *Phys. Rev. B*, 1996, **54**, 1703–1710.
11 H. Ouhbi and J. Wiktor, *J. Phys. Chem. C*, 2022, **126**, 19956–19961.
12 G. Miceli, W. Chen, I. Reshetnyak and A. Pasquarello, *Phys. Rev. B*, 2018, **97**, 121112.
13 T. Bischoff, I. Reshetnyak and A. Pasquarello, *Phys. Rev. B*, 2019, **99**, 201114.
14 T. Bischoff, J. Wiktor, W. Chen and A. Pasquarello, *Phys. Rev. Materials*, 2019, **3**, 123802.
15 M. Guidon, J. Hutter and J. VandeVondele, *J. Chem. Theory Comput.*, 2010, **6**, 2348–2364.
16 O. A. Vydrov and T. Van Voorhis, *The Journal of Chemical Physics*, 2010, **133**, 244103.
17 R. Sabatini, T. Gorni and S. De Gironcoli, *Phys. Rev. B*, 2013, **87**, 041108.
18 A. M. Ganose, M. Cuff, K. T. Butler, A. Walsh and D. O. Scanlon, *Chem. Mater.*, 2016, **28**, 1980–1984.
19 G. Kresse and J. Hafner, *Phys. Rev. B*, 1993, **47**, 558–561.
20 G. Kresse and J. Furthmüller, *Computational Materials Science*, 1996, **6**, 15–50.
21 G. Kresse and J. Furthmüller, *Phys. Rev. B*, 1996, **54**, 11169–11186.
22 S. Nosé, *The Journal of Chemical Physics*, 1984, **81**, 511–519.
23 W. G. Hoover, *Phys. Rev. A*, 1985, **31**, 1695–1697.
24 F. Ambrosio, G. Miceli and A. Pasquarello, *The Journal of Chemical Physics*, 2015, **143**, 244508.
25 F. Ambrosio, G. Miceli and A. Pasquarello, *J. Phys. Chem. Lett.*, 2017, **8**, 2055–2059.
26 S. Trasatti, *Pure and Applied Chemistry*, 1986, **58**, 955–966.